J Adv Ceram

Research Article

# Enhanced photocatalytic nitrogen fixation on ultrathin $Nb_2O_5{\cdot}nH_2O$ nanosheets in pure water through the synergistic effect of oxygen vacancies and acid sites

Xinzhu Qian[2], Xianpeng Liang[2], Taiyan Ding[1], Xing Ji[1], Junhao Shao[1], Siqiang Feng[1], Chunliang Zhou[3], Jianku Shang[2], Qi Li[1,✉]

Cite this article: Qian X, Liang X, Ding T, et al. *J Adv Ceram* 2025, **14**(5): 9221070. https://doi.org/10.26599/JAC.2025.9221070

**ABSTRACT:** Gaseous nitrogen is abundant in the atmosphere, and its efficient conversion to ammonia is vital to the future of a greener and more sustainable world. Since the N≡N covalent triple bond is difficult to break, the adsorption and activation of $N_2$ molecules on the photocatalyst surface are critical to improve the efficiency of photocatalytic nitrogen fixation. In this work, $Nb_2O_5{\cdot}nH_2O$ nanosheets were synthesized by a hydrothermal reduction process with a weak reducing agent of glyoxal, which created more oxygen vacancies on their surfaces. Furthermore, their surface acidity was modulated by subsequent heat treatment in an Ar atmosphere. Thus, the effects of the oxygen vacancy and surface acidity on the photocatalytic nitrogen fixation performance of these $Nb_2O_5{\cdot}nH_2O$ nanosheets could be investigated. It was found that both factors contributed to the adsorption/activation of $N_2$ and the charge carrier separation/transfer in these $Nb_2O_5{\cdot}nH_2O$ nanosheets. Owing to their synergistic effect, a high ammonia yield of 173.7 μmol/(g·h) was achieved by these $Nb_2O_5{\cdot}nH_2O$ nanosheets through photocatalysis in pure water under simulated solar illumination without assistance from either sacrificial agents or cocatalysts.

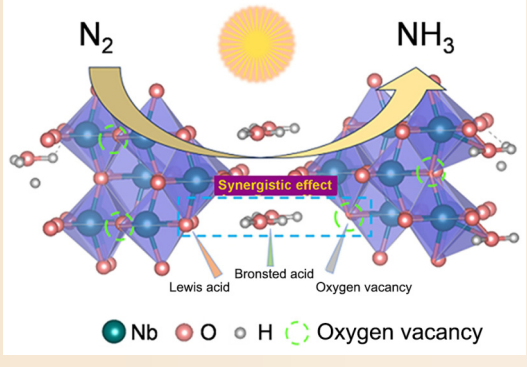


**KEYWORDS:** $Nb_2O_5{\cdot}nH_2O$ nanosheets; oxygen vacancies; acid sites; photocatalytic nitrogen fixation; $N_2$ adsorption and activation

## 1 Introduction

Ammonia can be utilized to produce soda ash, nitrogen fertilizer, and liquid nitrogen, which play vital roles in chemical, explosive, and fertilizer industries [1,2]. At present, the Haber–Bosch process with iron catalyst is still the main approach for industrial ammonia synthesis. However, its reaction conditions are extremely harsh, with high pressures (~15–25 MPa) and temperatures (~350–550 °C), which generally require high energy consumption from fossil fuel combustion. Thus, large amounts of $SO_2$ and $CO_2$ are produced in industrial ammonia synthesis globally, which causes serious atmospheric pollution and global warming problems [3,4]. Therefore, extensive research efforts have been committed to developing greener processes for efficient ammonia synthesis at ambient temperature and pressure [5,6].

Photocatalytic nitrogen fixation is believed to be a promising approach for greener ammonia synthesis because of its use of solar energy, mild reaction conditions, simple operation, and abundant photocatalyst resources [5]. Since its first report by Schrauzer and Guth in 1977 on the conversion of $N_2$ to $NH_3$ under sunlight irradiation with $TiO_2$ as the photocatalyst [7], a variety of semiconductor-based photocatalysts have been developed for successful photocatalytic nitrogen fixation, including CdS, BiOBr, $Fe_2TiO_5$, and $C_3N_4$ [8–11]. However, the application of photocatalytic nitrogen fixation is still limited till now because of its low efficiency. On one hand, the dissociation energy of N≡N triple bond in $N_2$ is as high as 941 kJ/mol, which makes it difficult to activate/cleave $N_2$ molecules and subsequently convert $N_2$ to $NH_3$ [12]. On the other hand, the recombination of photogenerated electrons and holes results in low charge carrier utilization, which in turn affects the overall photoreduction performance of $N_2$ [13]. Furthermore, the general requirement of hole sacrificial agents in photocatalytic nitrogen fixation increases the operation cost and complexity, which also hinders its potential application [12]. Thus, it is crucial to develop highly active photocatalysts for photocatalytic nitrogen fixation to overcome these limitations.

Defect engineering strategies have received enormous research

[1] Key Laboratory of Advanced Technologies of Materials (Ministry of Education), School of Materials Science and Engineering, Southwest Jiaotong University, Chengdu 610031, China. [2] Shenyang National Laboratory for Materials Science, Institute of Metal Research, Chinese Academy of Sciences, Shenyang 110016, China. [3] Yantai Research Institute, Harbin Engineering University, Yantai 264000, China.

✉ Corresponding author. E-mail: qiliuiuc@swjtu.edu.cn

Received: January 3, 2025; Revised: March 27, 2025; Accepted: March 29, 2025

attention in recent years to promote the efficiency of various photocatalytic reactions [14,15]. By constructing appropriate point defects on their surfaces [16], the charge density distributions on photocatalyst surfaces could be changed to enhance both the adsorption/activation of reactants and the separation of electron–hole pairs [13,14], both of which are beneficial for promoting their performance. For example, rich oxygen vacancies largely improved both the photogenerated charge carrier separation and $N_2$ adsorption/activation capabilities of $Bi_2MoO_6$ nanosheets, resulting in a largely enhanced photocatalytic nitrogen fixation performance [17]. Furthermore, the defect engineering strategy could also be combined with other material design strategies to obtain synergistic effects to further enhance the photocatalytic performance in various photocatalyst material systems, including elemental doping [18], plasmonic metallic deposition [19], and ferroelectricity [20].

Niobic-based oxides have been explored as solid acid catalysts, promoters, and redox materials in various catalytic reactions [21–23]. It has been reported that point defects associated with oxygen vacancies in $HNb_3O_8$ nanosheets enhance their adsorption and activation of $O_2$, which contributes to the improved activity of the photocatalytic oxidative coupling reaction of benzylamine under visible light irradiation [24]. Furthermore, niobic-based oxides have unique Lewis acid sites (LASs) and Bronsted acid sites (BASs), which could serve as electron acceptors to adsorb and activate certain gas molecules [21,25,26]. For example, the surface acidity of $Nb_2O_5$ has been reported to play important roles in promoting the photoreduction of $CO_2$ and the selective conversion of amines and alcohols [24,27,28]. Thus, if the defect engineering of oxygen vacancies and their unique surface acidity modulation approaches could be combined in niobic-based oxides, it might be beneficial for photocatalytic nitrogen fixation.

In this work, $Nb_2O_5{\cdot}nH_2O$ nanosheets were synthesized by a hydrothermal reduction process with a weak reducing agent of glyoxal to increase the concentration of oxygen vacancies on their surface. The enrichment of surface oxygen vacancies improved the separation and migration efficiency of photogenerated charge carriers and enhanced their adsorption and activation of $N_2$, both of which were beneficial for their good photocatalytic nitrogen fixation performance. The acidity of their surfaces also played an important role in the photocatalytic nitrogen fixation process through the enhancement of charge carrier separation/transfer and $N_2$ adsorption/activation. When their surface acidity decreased, their $NH_4^+$ production efficiency decreased accordingly. Thus, the synergistic effect of oxygen vacancies and acid sites in these $Nb_2O_5{\cdot}nH_2O$ nanosheets resulted in a high $NH_4^+$ yield of ~173.7 μmol/(g·h) in pure water under simulated solar illumination without the assistance of either sacrificial agents or cocatalysts.

## 2 Experimental

### 2.1 Chemicals and materials

Niobium chloride ($NbCl_5$, 99%) and glyoxal solution ($C_2H_2O_2$, 40 wt% in $H_2O$) were purchased from Shanghai Macklin Biochemical Co., Ltd., China. Absolute ethanol ($C_2H_5OH$, 99.7%), ammonia ($NH_3{\cdot}H_2O$, 25 wt%), Nessler ($K_2HgI_4$), potassium sodium tartrate tetrahydrate ($C_4H_4KNaO_6{\cdot}4H_2O$, 99%), hydrochloric acid (HCl, 38%), methanol ($CH_3OH$, 99.7%), ammonium chloride ($NH_4Cl$, 99.8%), 2-methylbenzaldehyde ($C_9H_{10}O$, 97%), hydrazine hydrochloride ($N_2H_4{\cdot}2HCl$, 98%), and sodium sulfate ($Na_2SO_4$, 99%) were purchased from Sinopharm Chemical Reagent Co., Ltd., China. High purity $N_2$ (> 99.999%) and high purity Ar (> 99.999%) were supplied by Dalian Special Gases Gas Co., Ltd., China. 1-Methyl-2-pyrrolidinone (> 99.5%) and polyvinylidene fluoride (PVDF) were purchased from Aladdin Chemistry Co., Ltd., China. The water used in all the experiments was ultrapure water. All of the chemicals were used without further purification.

### 2.2 Synthesis of ultrathin $Nb_2O_5{\cdot}nH_2O$ nanosheets

Ultrathin $Nb_2O_5{\cdot}nH_2O$ nanosheets were synthesized by one-step hydrothermal process according to a previous study [29]. First, 400 mg $NbCl_5$ was dissolved in 10 mL ethanol under magnetic stirring for 30 min. Then, 40 mL $H_2O$ and 8 mL $NH_3{\cdot}H_2O$ were added into $NbCl_5$ ethanol solution in turn. After the mixture was aged for several hours at room temperature, the precipitate was separated by centrifugation and sealed in a 100 mL Teflon-lined stainless-steel autoclave pre-filled with 50 mL distilled water. Hydrothermal reaction was carried out at 180 °C for 24 h. After being cooled down to room temperature naturally, the obtained product was collected, washed with ethanol and deionized water in sequence several times, and freeze-dried for 24 h to obtain ultrathin $Nb_2O_5{\cdot}nH_2O$ nanosheets ($Nb_2O_5{\cdot}nH_2O$ sample).

### 2.3 Synthesis of oxygen-deficient $Nb_2O_5{\cdot}nH_2O$ nanosheets and oxygen-deficient $Nb_2O_5{\cdot}nH_2O$ nanosheets with different surface acidities

Hydrothermal reduction process was carried out to enrich the presence of oxygen vacancies on the surface of $Nb_2O_5{\cdot}nH_2O$ nanosheets with a weak reducing agent of glyoxal. 100 mg of as-prepared $Nb_2O_5{\cdot}nH_2O$ nanosheets and different amounts of glyoxal (1, 2, and 3 mL) were mixed in 30 mL DI water via ultrasonication. Then, the mixture was transferred to a 50 mL Teflon-lined autoclave and heated at 100 °C for 6 h. After cooling to room temperature naturally, the obtained product was collected, washed with ethanol and deionized water in sequence several times, and freeze-dried for 24 h to obtain $V_O$-$Nb_2O_5{\cdot}nH_2O$-*X* samples (*X* represents the amount of added glyoxal in millilitre). To explore the effect of surface acidity on their photocatalytic nitrogen fixation performance, the $V_O$-$Nb_2O_5{\cdot}nH_2O$-2 sample was annealed at 150, 200, and 300 °C respectively, for 1 h in an argon atmosphere, and the obtained samples were named $V_O$-$Nb_2O_5{\cdot}nH_2O$-2-*Y* samples (*Y* represents the annealing temperature in °C).

### 2.4 Material characterization

A D8 ADVANCE powder X-ray diffractometer (XRD; Bruker Co., Germany) was used to conduct qualitative and semi-quantitative analyses of the crystal structure and unit cell parameters of prepared samples. A SUPRA55 field emission scanning electron microscope (FESEM; Carl Zeiss NTS GmbH, Germany) was utilized. Before imaging, the fully dried sample was sputtered with gold for 120 s in a K575 high-precision sputtering coater to enhance its surface conductivity. A Tecnai G2 F20 transmission electron microscope (TEM, USA) was used to observe the lattice structure and morphology of prepared catalysts. The chemical valence state, semi-quantitative atomic percentage, and surface element composition of samples were analyzed by an ESCALAB250 X-ray photoelectron spectrometer (XPS; Thermo, USA). The structure of the prepared catalysts was characterized by a CORA 5200 Fiber Raman spectrometer (Anton Paar Inc., Germany). Ultraviolet–visible (UV–vis) diffuse reflectance spectra of the samples were recorded with a UV-2550 spectrophotometer (Shimadzu Corporation, Japan) to obtain their optical absorbance

spectra. Mott–Schottky curves, electrochemical impedance spectroscopy (EIS), and photocurrent transient response tests were performed on a three-electrode system using a CHI 660E electrochemical workstation (CI Instruments, China). Nafion-prepared electrode films, platinum wires, and Ag/AgCl were used as the working electrode, counter electrode, and reference electrode, respectively. A 0.2 M $Na_2SO_4$ solution served as the electrolyte. Fourier transform infrared (FT-IR) spectra were recorded by a Bruker Tensor 27 FT-IR spectrometer with the measuring range between 350 and 4000 $cm^{-1}$. Electron paramagnetic resonance (EPR) spectra of the samples were recorded to confirm the presence of oxygen vacancies via an electron spin resonance (EPR) spectrometer (Bruker A300, Bruker Corporation, Germany). The measurement frequency was 9.60 GHz, and the temperature was −196 °C. $N_2$ temperature-programmed desorption ($N_2$-TPD) analysis was performed on a Micromeritics Auto Chem 2920 II instrument (USA) to explore the $N_2$ adsorption capacity of the samples.

### 2.5 Photocatalytic $N_2$ reduction experiment

The photocatalytic nitrogen fixation experiment was carried out in a closed quartz reactor equipped with a circulating water-cooling system. Typically, 50 mg of photocatalyst was suspended in 80 mL of ultra-pure water, and high-purity $N_2$ gas (99.99%) was continuously bubbled through the suspension at a rate of 60 mL/min for 30 min. Next, the photocatalyst suspension was continuously stirred in dark for 30 min to reach adsorption/desorption equilibrium before illumination was switched on. A 300 W Xe lamp (PLSSXE300, Perfectlight Technology Co., Ltd., China, light intensity ≈ 100 mW/$cm^2$) was used as the simulated solar light illumination source. Every 30 min, 5 mL of the suspension was collected using a syringe, immediately filtered through a 0.2 μm membrane, and centrifuged to separate the photocatalyst. The concentrations of $NH_4^+$ and $N_2H_4$ products were spectrophotometrically determined via Nessler's reagent method [30] and para-dimethylaminobenzaldehyde [31], respectively, with a UV-2550 spectrometer (Shimadzu, Japan). To assess the stability and recyclability of the sample, cyclic photocatalytic nitrogen fixation experiments were performed. The cyclic experiments were conducted for 5 consecutive runs. After each usage, the sample was collected, washed with deionized (DI) water, subjected to a hydrothermal reduction process, and dried. The dried sample was then used for the next run with the same sample concentration.

## 3 Results and discussion

### 3.1 Crystal structure and morphology of samples

The sample preparation process is schematically shown in Fig. 1. $Nb_2O_5{\cdot}nH_2O$ nanosheets were synthesized by a hydrothermal process adopted from Ref. [29], and then a hydrothermal reduction process with a weak reducing agent of glyoxal created oxygen vacancies on their surface to generate $V_O$-$Nb_2O_5{\cdot}nH_2O$-X samples. Further heat treatments on the $V_O$-$Nb_2O_5{\cdot}nH_2O$-2 samples in an Ar atmosphere at various temperatures (150, 200, and 300 °C) were conducted to modulate their surface acidity. Figure 2(a) shows the XRD diffraction patterns of $Nb_2O_5{\cdot}nH_2O$, $V_O$-$Nb_2O_5{\cdot}nH_2O$-1, $V_O$-$Nb_2O_5{\cdot}nH_2O$-2, $V_O$-$Nb_2O_5{\cdot}nH_2O$-3, and $V_O$-$Nb_2O_5{\cdot}nH_2O$-2-300 samples. Except for the $V_O$-$Nb_2O_5{\cdot}nH_2O$-2-300 sample, all other samples presented three clear XRD diffraction peaks at 2$\theta$ angles of ~6°, ~25°, and ~52°, respectively, which could be attributed to the layer structure characteristics, (140) diffraction peak, and (240) diffraction peak of $Nb_2O_5{\cdot}nH_2O$ nanosheets [29]. This observation indicated that the hydrothermal reduction process used to create oxygen vacancies did not cause changes in the crystal structure of these samples. The $V_O$-$Nb_2O_5{\cdot}nH_2O$-2-300 sample also had the same two XRD diffraction peaks at 2$\theta$ values of ~25° and ~52°, while the other

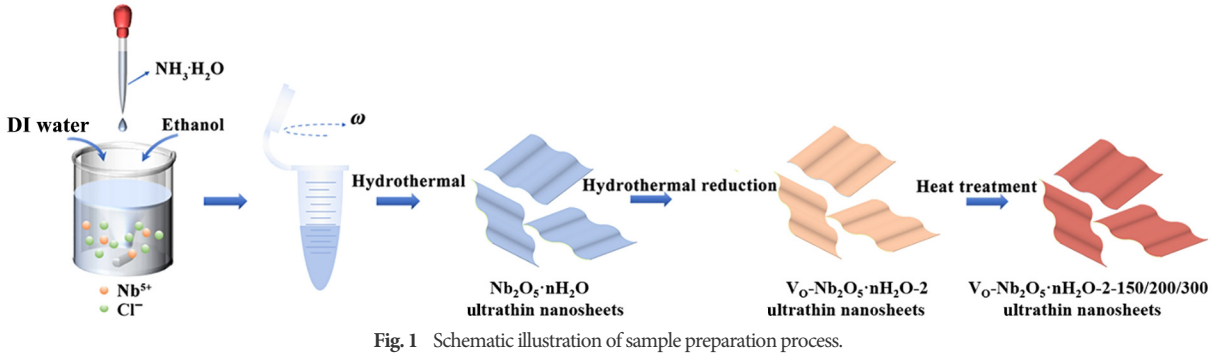


**Fig. 1** Schematic illustration of sample preparation process.

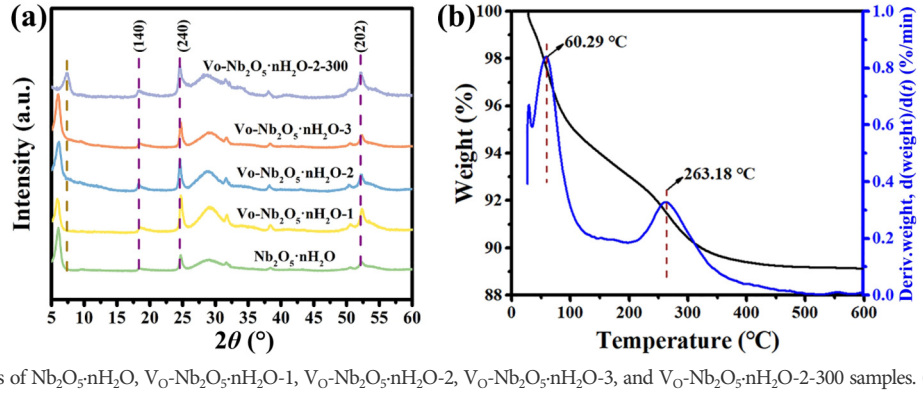


**Fig. 2** (a) XRD patterns of $Nb_2O_5{\cdot}nH_2O$, $V_O$-$Nb_2O_5{\cdot}nH_2O$-1, $V_O$-$Nb_2O_5{\cdot}nH_2O$-2, $V_O$-$Nb_2O_5{\cdot}nH_2O$-3, and $V_O$-$Nb_2O_5{\cdot}nH_2O$-2-300 samples. (b) TG analysis results of $Nb_2O_5{\cdot}nH_2O$ sample.

XRD diffraction peak shifted from 2$\theta$ of ~6° to ~7.5°. This shift in the higher 2$\theta$ direction indicated a decrease in the $d$ value of the layer spacing, which could be attributed to interlayer dehydration occurring during further heat treatment [32]. Figure 2(b) shows the thermogravimetric (TG) analysis results for the $Nb_2O_5{\cdot}nH_2O$ sample, which demonstrated that water loss occurred in low- and high-temperature regions. From the weight loss data, $n$ could be determined to be ~1.5 for the $Nb_2O_5{\cdot}nH_2O$ sample.

The morphologies and crystal structures of samples were characterized by SEM and TEM. Figures 3(a)–3(c) show representative FESEM images of $Nb_2O_5{\cdot}nH_2O$, $V_O$-$Nb_2O_5{\cdot}nH_2O$-2, and $V_O$-$Nb_2O_5{\cdot}nH_2O$-2-300 samples, respectively, which demonstrated that the $Nb_2O_5{\cdot}nH_2O$ sample synthesized by the hydrothermal process had a nanosheet morphology and did not change after hydrothermal reduction to create oxygen vacancies or even after further heat treatment in an Ar atmosphere. Figure 3(d) shows the TEM image of the $V_O$-$Nb_2O_5{\cdot}nH_2O$-2 sample as a representative of other samples, which further demonstrated its nanosheet structure. At the edge of these nanosheets, the very light color indicated their ultrathin nature. Figure 3(e) shows the high-resolution TEM (HRTEM) image of one nanosheet of the $V_O$-$Nb_2O_5{\cdot}nH_2O$-2 sample, which clearly demonstrated its crystalline nature. Two sets of lattice fringes could be clearly observed with lattice spacing $d$ values of ~0.295 and ~0.313 nm, which were similar to the lattice spacing $d$ values of the (320) and (041) planes of the orthorhombic-phase $H_3ONb_3O_8$ nanosheets [29]. Figure 3(f) shows the selected area electron diffraction pattern of one nanosheet of the $V_O$-$Nb_2O_5{\cdot}nH_2O$-2 sample, which demonstrated that its diffraction rings were continuous with a relatively uniform contrast distribution. Thus, the $V_O$-$Nb_2O_5{\cdot}nH_2O$-2 sample had a polycrystalline nature, and there was no preferential orientation in the nucleation and grain growth process. Similar to its HRTEM image, its diffraction rings were similar to those of the orthorhombic-phase $H_3ONb_3O_8$ nanosheet, which was consistent with Ref. [29].

### 3.2 Composition, oxygen vacancy, and acidity analysis of samples

X-ray photoelectron spectroscopy (XPS) was used to explore the element valence states and oxygen species in these samples. Figures 4(a)–4(c) show the XPS survey spectrum, high-resolution O 1s XPS spectra, and high-resolution Nb 3d XPS spectra of the $V_O$-$Nb_2O_5{\cdot}nH_2O$-2 sample as a representative of these samples, respectively, and the XPS analysis results of other samples can be found in Fig. S1 in the Electronic Supplementary Material (ESM). Figure 4(a) shows the existence of XPS peaks of Nb, O, and C elements. Nb and O signals came from the sample, while the C 1s peak came from widespread carbon in the environment. Its high-resolution O 1s XPS spectrum could be best fitted by the

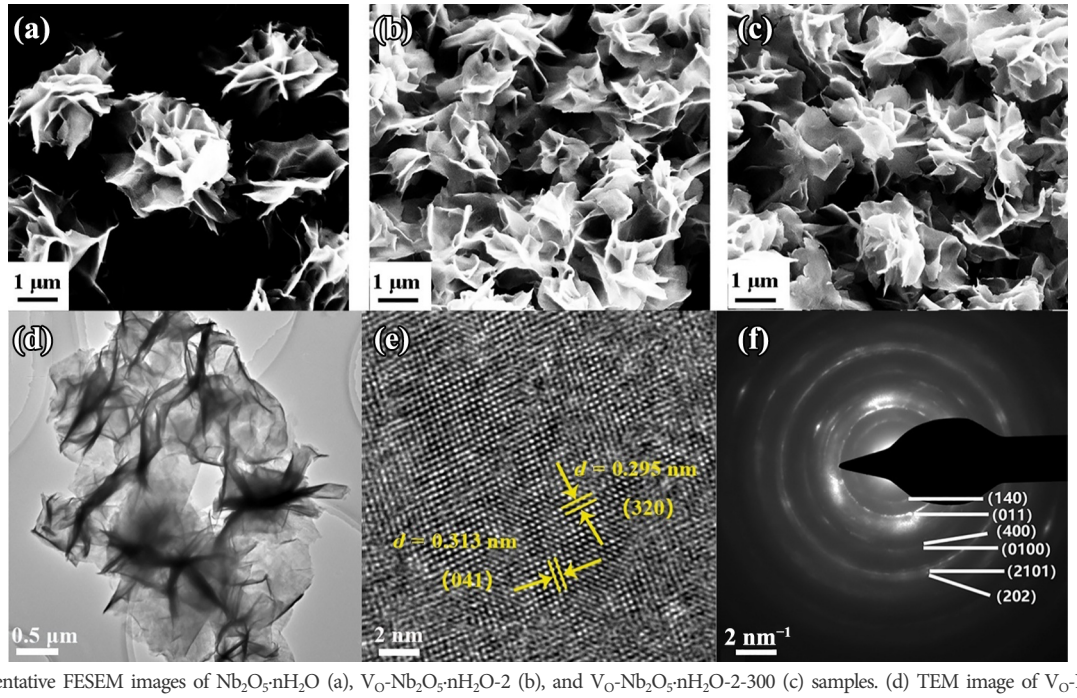


**Fig. 3** Representative FESEM images of $Nb_2O_5{\cdot}nH_2O$ (a), $V_O$-$Nb_2O_5{\cdot}nH_2O$-2 (b), and $V_O$-$Nb_2O_5{\cdot}nH_2O$-2-300 (c) samples. (d) TEM image of $V_O$-$Nb_2O_5{\cdot}nH_2O$-2 sample. (e) HRTEM image of one nanosheet of $V_O$-$Nb_2O_5{\cdot}nH_2O$-2 sample. (f) Selected area electron diffraction pattern of one nanosheet of $V_O$-$Nb_2O_5{\cdot}nH_2O$-2 sample.

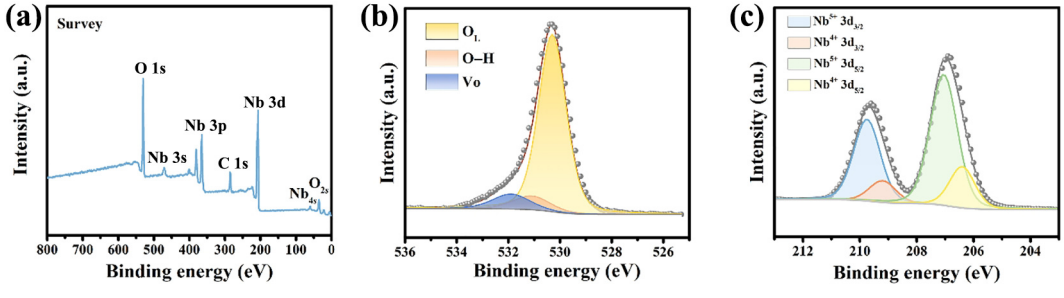


**Fig. 4** (a) XPS survey spectrum, (b) high-resolution O 1s XPS spectrum, and (c) high-resolution Nb 3d XPS spectrum of $V_O$-$Nb_2O_5{\cdot}nH_2O$-2 sample.

combination of three peaks located at ~530.3, ~531.1, and ~531.9 eV for lattice oxygen ($O_L$), –OH, and oxygen vacancies ($V_O$), respectively [24,33,34]. Its high-resolution Nb 3d XPS spectra could be best fitted with the combination of four peaks. The two peaks at ~209.9 and ~207.1 eV could be assigned to $Nb^{5+}$ $3d_{3/2}$ and $Nb^{5+}$ $3d_{5/2}$ peaks, while the other two peaks at ~209.2 and ~206.3 eV could be assigned to $Nb^{4+}$ $3d_{3/2}$ and $Nb^{4+}$ $3d_{5/2}$ peaks [33]. The occurrence of $Nb^{4+}$ signals was consistent with the generation of oxygen vacancies.

Table 1 summarizes the XPS analysis results of these samples. With increasing amounts of the reducing agent of glyoxal from 1 to 3 mL to produce $V_O$-$Nb_2O_5{\cdot}nH_2O$-X samples, their oxygen vacancy percentages increased from ~6.26% to ~12.37%, all of which were obviously higher than that of the $Nb_2O_5{\cdot}nH_2O$ sample at ~4.29%. Their $Nb^{4+}/Nb^{5+}$ percentages increased from ~13.29% to ~21.81%, all of which were obviously higher than that of the $Nb_2O_5{\cdot}nH_2O$ sample at ~6.36%. Thus, the hydrothermal reduction process did create oxygen vacancies on these $Nb_2O_5{\cdot}nH_2O$ nanosheets. Moreover, their acidity did not change much during the hydrothermal reduction process. The surface -OH percentage of the $Nb_2O_5{\cdot}nH_2O$ sample was ~7.65%, while those of the $V_O$-$Nb_2O_5{\cdot}nH_2O$-X samples were ~8.17%, ~8.62%, and ~8.19%, respectively. In contrast, further heat treatment in an Ar atmosphere did not significantly change the percentage of oxygen vacancies. For example, the percentages of oxygen vacancies and $Nb^{4+}/Nb^{5+}$ of the $V_O$-$Nb_2O_5{\cdot}nH_2O$-2-300 sample were ~9.86% and 18.87%, respectively, which are close to those of the $V_O$-$Nb_2O_5{\cdot}nH_2O$-2 sample (~9.32% and ~17.37%). However, its surface -OH percentage largely decreased to ~4.33%, almost only half of that of the $V_O$-$Nb_2O_5{\cdot}nH_2O$-2 sample without heat treatment. Thus, the oxygen vacancy concentration and surface acidity of these samples could be modulated as designed.

To further verify the existence of oxygen vacancies in these samples, EPR analysis was used [35]. Figure 5(a) shows the EPR spectra of the pristine $Nb_2O_5{\cdot}nH_2O$ sample and $V_O$-$Nb_2O_5{\cdot}nH_2O$-2 sample. A strong EPR signal peak at $g$ = 2.003 emerged after the hydrothermal reduction, which indicated the abundance of oxygen vacancies in the $V_O$-$Nb_2O_5{\cdot}nH_2O$-2 sample [33]. Figure 5(b) shows the Raman spectra of $Nb_2O_5{\cdot}nH_2O$, $V_O$-$Nb_2O_5{\cdot}nH_2O$-2, and $V_O$-$Nb_2O_5{\cdot}nH_2O$-2-300 samples. In general, the Raman peak between 200 and 400 $cm^{-1}$ can be assigned to the bending vibration of Nb–O–Nb; the Raman peak between 400 and 700 $cm^{-1}$ is related to the tensile vibration of $NbO_6$, and the Raman peak at ~900 $cm^{-1}$ is related to the asymmetric tensile vibration of Nb=O bond at the terminal [36]. After the creation of oxygen vacancies, these characteristic peaks in $V_O$-$Nb_2O_5{\cdot}nH_2O$-2 and $V_O$-$Nb_2O_5{\cdot}nH_2O$-2-300 samples broadened with much lower intensities than those in the $Nb_2O_5{\cdot}nH_2O$ sample, indicating that

**Table 1** XPS analysis results of $Nb_2O_5{\cdot}nH_2O$, $V_O$-$Nb_2O_5{\cdot}nH_2O$-1, $V_O$-$Nb_2O_5{\cdot}nH_2O$-2, $V_O$-$Nb_2O_5{\cdot}nH_2O$-3, and $V_O$-$Nb_2O_5{\cdot}nH_2O$-2-300 samples

| Sample | $O_L$ (%) | –OH (%) | $O_v$ (%) | $Nb^{4+}/Nb^{5+}$ (%) |
|---|---|---|---|---|
| $Nb_2O_5{\cdot}nH_2O$ | 88.06 | 7.65 | 4.29 | 6.36 |
| Vo-$Nb_2O_5{\cdot}nH_2O$-1 | 85.57 | 8.17 | 6.26 | 13.29 |
| Vo-$Nb_2O_5{\cdot}nH_2O$-2 | 82.06 | 8.62 | 9.32 | 17.37 |
| Vo-$Nb_2O_5{\cdot}nH_2O$-3 | 79.44 | 8.19 | 12.37 | 21.81 |
| Vo-$Nb_2O_5{\cdot}nH_2O$-2-300 | 85.81 | 4.33 | 9.86 | 18.87 |

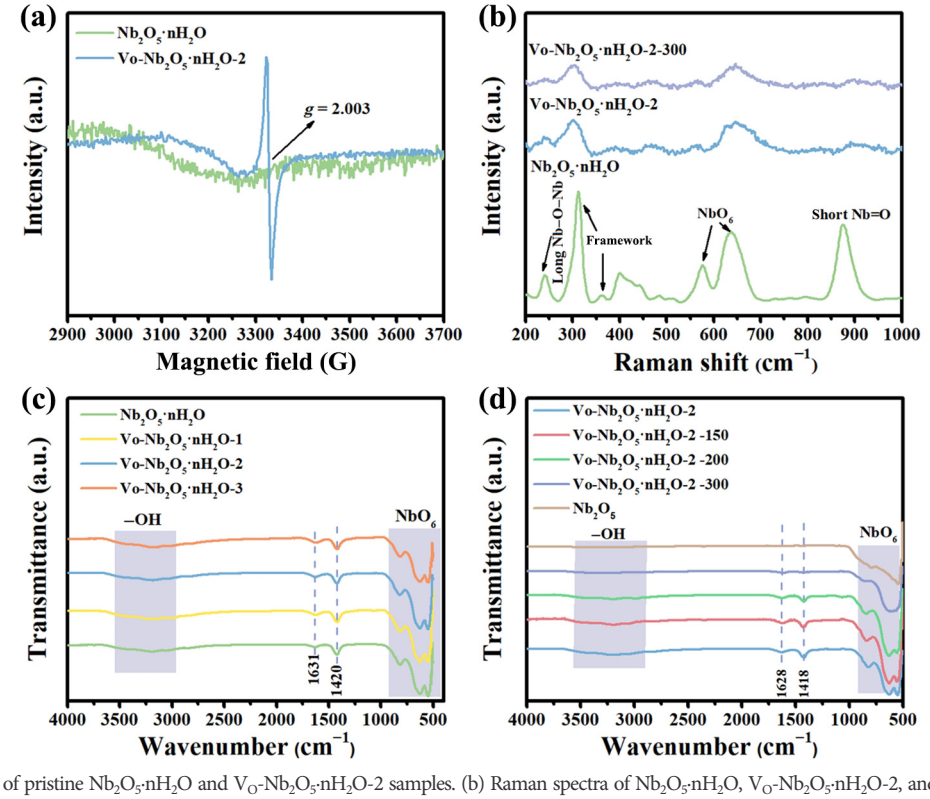


**Fig. 5** (a) EPR spectra of pristine $Nb_2O_5{\cdot}nH_2O$ and $V_O$-$Nb_2O_5{\cdot}nH_2O$-2 samples. (b) Raman spectra of $Nb_2O_5{\cdot}nH_2O$, $V_O$-$Nb_2O_5{\cdot}nH_2O$-2, and $V_O$-$Nb_2O_5{\cdot}nH_2O$-2-300 samples. (c) FT-IR spectra of $Nb_2O_5{\cdot}nH_2O$ and $V_O$-$Nb_2O_5{\cdot}nH_2O$-*X* samples. (d) FT-IR spectra of $V_O$-$Nb_2O_5{\cdot}nH_2O$-2-*Y* samples.

their crystal lattices were distorted after hydrothermal reduction from the creation of oxygen vacancies.

Figure 5(c) compares the FT-IR spectra of $Nb_2O_5{\cdot}nH_2O$ and $V_O$-$Nb_2O_5{\cdot}nH_2O$-X samples. After hydrothermal reduction treatment with different reducing agent concentrations, their peak positions and peak intensities were generally the same as those of the pristine $Nb_2O_5{\cdot}nH_2O$ sample. The bands centered at ~3200 and ~1631 $cm^{-1}$ could be assigned to the stretching and bending vibrations of surface hydroxyl groups (Bronsted acid sites), respectively [37], the band at ~1420 $cm^{-1}$ Lewis acid sites in $Nb_2O_5{\cdot}nH_2O$ [38,39], and the bands between 800 and 400 $cm^{-1}$ the vibration of $NbO_6$ octahedron [40]. Thus, the hydrothermal reduction treatment did not cause obvious changes in the surface groups or acidity of $V_O$-$Nb_2O_5{\cdot}nH_2O$-*X* samples, which was consistent with the XPS analysis results. Figure 5(d) shows the FT-IR spectra of $V_O$-$Nb_2O_5{\cdot}nH_2O$-2-*Y* samples, which clearly demonstrates that the peak intensities of the stretching/bending vibrations of surface hydroxyl groups and Lewis acid sites became increasingly weak with increasing heat treatment temperature. This observation was also consistent with the XPS analysis results. Thus, heat treatment weakened the surface acidity of the sample, which was similar to the observations of Florentino *et al.* [41] that the heat treatment of a niobic acid catalyst caused the elimination of water and a decrease in acid site strength.

### 3.3 Optical properties and band structures of samples

The optical properties of the samples were investigated via UV–visible diffuse reflectance spectroscopy. Figure 6(a) shows the light absorption curves of these samples approximated by the Kubelka–Munk function [42], and Fig. 6(b) shows their Tauc plots ($(\alpha hv)^{0.5}$ vs. $hv$) to determine their band gap values [43]. All the samples presented a major light response within the UV region. The absorption stopping edge of the $Nb_2O_5{\cdot}nH_2O$ sample was at ~320 nm, and its corresponding band gap value was determined to be ~3.84 eV. After hydrothermal reduction, slight absorption redshifts were observed for the $V_O$-$Nb_2O_5{\cdot}nH_2O$-*X* samples, and their band gap values were determined to be ~3.75, ~3.71, and ~3.68 eV, respectively. Furthermore, they exhibited absorption tails far into the visible light region, which could be attributed to defect energy levels introduced into their band gaps due to oxygen vacancies for the visible light response [44,45].

Figure 6(c) shows the Mott–Schottky (M–S) curves of these samples, which demonstrated that their M–S curves had positive slopes. Thus, they had the n-type semiconductor nature, as expected [46]. The flat band potentials vs. the Ag/AgCl electrode at pH 7 were determined to be ~–0.66, ~–0.56, ~–0.52, and ~–0.49 V for $Nb_2O_5{\cdot}nH_2O$, $V_O$-$Nb_2O_5{\cdot}nH_2O$-1, $V_O$-$Nb_2O_5{\cdot}nH_2O$-2, and $V_O$-$Nb_2O_5{\cdot}nH_2O$-3 samples, respectively. For n-type semiconductors, their flat band potential is generally ~0.2 V more positive than their conduction band minimum (CBM) [47]. Therefore, their CBMs vs. the normal hydrogen electrode (NHE) could be calculated to be ~–0.64, ~–0.54, ~–0.50, and ~–0.47 V, respectively. Thus, their valence band maximum (VBM) values vs. NHE could be calculated based on their band gap values and CBM values at ~3.20, ~3.21, ~3.21, and ~3.21 V, respectively. Figure 6(d) shows their schematic energy band structures. Compared with the pristine $Nb_2O_5{\cdot}nH_2O$ sample, the introduction of oxygen vacancies positively shifted the conduction band bottoms of $V_O$-$Nb_2O_5{\cdot}nH_2O$-*X* samples, while their valence band tops did not change obviously.

### 3.4 Photocatalytic $N_2$ fixation performance under simulated sunlight illumination

The nitrogen fixation performance of the samples was explored under simulated solar irradiation in pure water without any sacrificial agent or cocatalyst, and the light intensity was ~100 mW/$cm^2$. The concentration of ammonia generated in the photocatalytic nitrogen fixation process was determined by UV–vis spectrophotometry with Nessler's reagent [24]. Figure S2(a) in the ESM shows the calibration curve between the ammonia concentration and the solution light absorbance with Nessler's reagent, which demonstrated a linear relationship with a high correlation coefficient $R^2$ of 0.9998. The closeness of its $R^2$ value to 1 demonstrated that the linear equation had a highly accurate fitting of the experimental data.

Figure 7(a) compares the photocatalytic ammonia production by $Nb_2O_5{\cdot}nH_2O$ and $V_O$-$Nb_2O_5{\cdot}nH_2O$-*X* samples, which had

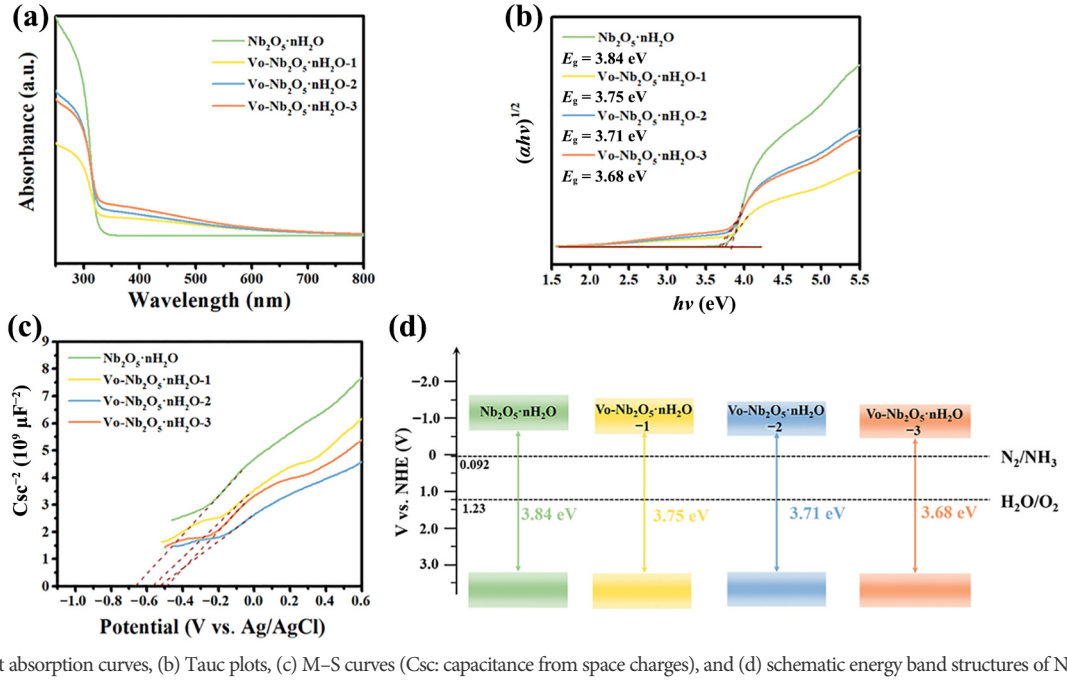


**Fig. 6** (a) Light absorption curves, (b) Tauc plots, (c) M–S curves (Csc: capacitance from space charges), and (d) schematic energy band structures of $Nb_2O_5{\cdot}nH_2O$ and $V_O$-$Nb_2O_5{\cdot}nH_2O$-*X* samples.

similar surface acidities and different oxygen vacancy concentrations. All of them demonstrated continuous production of ammonium under simulated solar irradiation, while they possessed very different photocatalytic $N_2$ reduction performances. The production of ammonia was closely related to the oxygen vacancy concentration. With increasing oxygen vacancy concentration from ~4.29% in the $Nb_2O_5{\cdot}nH_2O$ sample to ~6.26% in the $V_O$-$Nb_2O_5{\cdot}nH_2O$-1 sample and to ~9.32% in the $V_O$-$Nb_2O_5{\cdot}nH_2O$-2 sample, the production of ammonia increased from ~88 to ~218.9 and to ~347.5 μmol/g after 2 h of treatment, respectively. The production of ammonia by the $V_O$-$Nb_2O_5{\cdot}nH_2O$-2 sample was ~3.95 times that of the $Nb_2O_5{\cdot}nH_2O$ sample. When the oxygen vacancy concentration further increased to ~12.37%, the production of ammonia by the $V_O$-$Nb_2O_5{\cdot}nH_2O$-3 sample sharply decreased to ~167.5 μmol/g after 2 h of treatment, which was only approximately half of that of the $V_O$-$Nb_2O_5{\cdot}nH_2O$-2 sample. Thus, there was an optimized oxygen vacancy concentration in these samples to obtain the best photocatalytic ammonia production performance.

Figure 7(b) shows the photocatalytic ammonia production by $V_O$-$Nb_2O_5{\cdot}nH_2O$-2-Y samples, which had similar oxygen vacancy concentrations and different surface acidities. All of them demonstrated continuous production of ammonium under simulated solar irradiation, while their photocatalytic $N_2$ reduction performance gradually deteriorated with increasing annealing temperature (decreasing surface acidity). When the surface acidity decreased from ~8.62% (–OH concentration) in the $V_O$-$Nb_2O_5{\cdot}nH_2O$-2 sample to ~4.33% (–OH concentration) in the $V_O$-$Nb_2O_5{\cdot}nH_2O$-2-300 sample, the production of ammonia after 2 h of treatment decreased from ~347.5 to ~102.2 μmol/g, representing a large loss of ~75%.

To verify that the production of ammonia was derived from photocatalytic $N_2$ reduction, a series of control experiments in an argon atmosphere with the $V_O$-$Nb_2O_5{\cdot}nH_2O$-2 sample, in a $N_2$ atmosphere without photocatalyst, and in dark with the $V_O$-$Nb_2O_5{\cdot}nH_2O$-2 sample were conducted. Figure 7(c) shows the average ammonia production rates after 2 h of treatment, which demonstrated that ammonia production in these control experiments was negligible compared with that of the $V_O$-$Nb_2O_5{\cdot}nH_2O$-2 sample in a $N_2$ atmosphere under simulated solar irradiation (~173.7 μmol/(g·h)). The minimal ammonia production in these control experiments could be attributed to some residual air in the reactor or some dissolved nitrogen in the water [48]. Thus, these control experiments demonstrated that the production of ammonia by the $V_O$-$Nb_2O_5{\cdot}nH_2O$-2 sample under simulated solar illumination was derived from its photocatalytic $N_2$ reduction.

To explore the ammonia production pathway by the $V_O$-$Nb_2O_5{\cdot}nH_2O$-2 sample, the production of $N_2H_4$ in the photocatalytic nitrogen fixation process was examined. Figure S2(b) in the ESM shows the calibration curve between the $N_2H_4$ concentration and solution light absorbance via p-dimethylaminobenzaldehyde colorimetry [31], which demonstrated a linear relationship with a high correlation coefficient $R^2$ of 0.9995. The closeness of the $R^2$ value to 1 demonstrated that the linear equation had a highly accurate fitting of the experimental data. Figure 7(d) shows that no $N_2H_4$ was produced during the photocatalytic $N_2$ fixation process by the $V_O$-$Nb_2O_5{\cdot}nH_2O$-2 sample, which suggested that the reaction pathway of $N_2$ on the surface of the $V_O$-$Nb_2O_5{\cdot}nH_2O$-2 sample during the photocatalytic $N_2$ fixation reaction was the distal associative pathway by hydrogenation at one end of the nitrogen molecule, and no hydrogenation at either end occurred. This observation was consistent with Refs. [49–52].

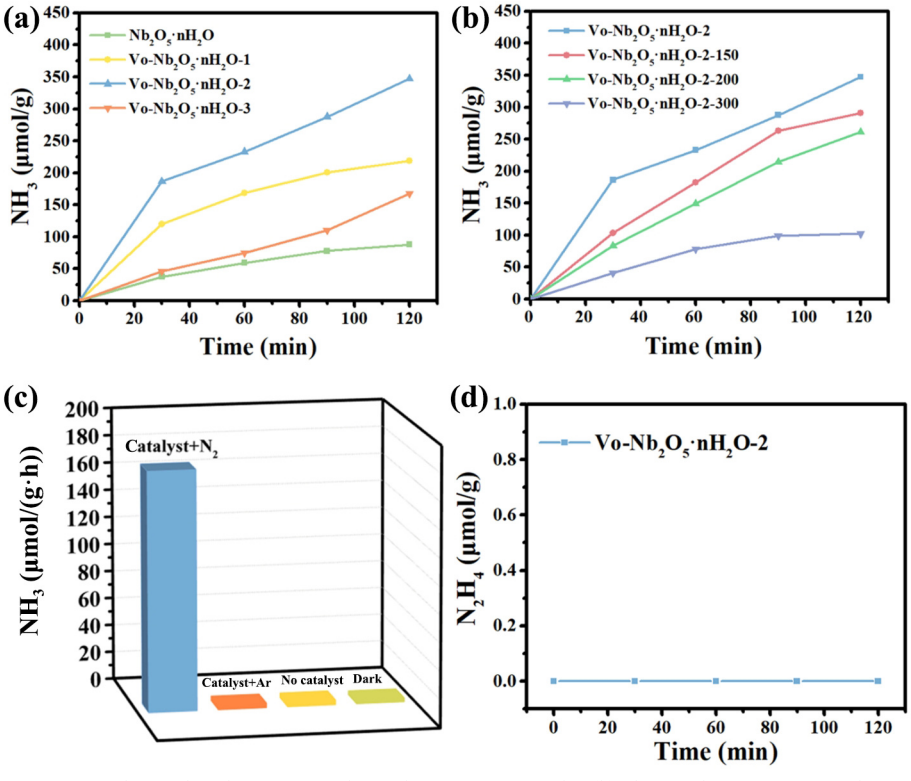


**Fig. 7** (a) Photocatalytic ammonia production by $Nb_2O_5{\cdot}nH_2O$ and $V_O$-$Nb_2O_5{\cdot}nH_2O$-*X* samples. (b) Photocatalytic ammonia production by $V_O$-$Nb_2O_5{\cdot}nH_2O$-2-*Y* samples. (c) Average ammonia production rates after 2 h treatment of $V_O$-$Nb_2O_5{\cdot}nH_2O$-2 samples in a $N_2$ atmosphere under simulated solar irradiation, in an argon atmosphere under simulated solar irradiation, in a $N_2$ atmosphere in dark, and $N_2$ atmosphere under simulated solar irradiation without a photocatalyst. (d) Photocatalytic $N_2H_4$ production by $V_O$-$Nb_2O_5{\cdot}nH_2O$-2 sample.

Table 2 summarizes the photocatalytic nitrogen fixation performances of various photocatalysts reported in Refs. [51–60], which were then compared with that of our $V_O$-$Nb_2O_5$·$nH_2O$-2 sample. The average ammonia production rate of the $V_O$-$Nb_2O_5$·$nH_2O$-2 sample reached ~173.7 μmol/(g·h) in pure water without the assistance of any sacrificial agent or cocatalysts, which was even higher than that of some reported photocatalysts with sacrificial agents or cocatalysts. A proper amount of oxygen vacancies and acid sites in the $V_O$-$Nb_2O_5$·$nH_2O$-2 sample were found to be critical for its good photocatalytic nitrogen fixation performance.

### 3.5 Regeneration and reusability of $V_O$-$Nb_2O_5$·$nH_2O$-2 sample in the photocatalytic nitrogen fixation process

The oxygen vacancies in the $V_O$-$Nb_2O_5$·$nH_2O$-2 sample were partially consumed during the photocatalytic nitrogen fixation process. Thus, a regeneration process was developed after the sample was used, which included separation and collection, washing and drying, and hydrothermal reduction by glyoxal to regenerate oxygen vacancies. Figure 8(a) shows the XRD pattern of the $V_O$-$Nb_2O_5$·$nH_2O$-2 sample after five consecutive cycles. No significant difference was observed in its XRD pattern compared with that of its fresh state. There was only a slight XRD diffraction peak shift at $2\theta \approx 6°$ in the lower $2\theta$ direction, which indicated that a slight layer distance increase occurred in these $Nb_2O_5$·$nH_2O$ nanosheets during the photocatalytic reaction and regeneration process cycles. Figure 8(b) shows the SEM image of the $V_O$-$Nb_2O_5$·$nH_2O$-2 sample after five consecutive cycles, which indicated that it also retained its nanosheet morphology during the photocatalytic reaction and regeneration process cycles. The Brunauer–Emmett–Teller (BET) specific area of the $V_O$-$Nb_2O_5$·$nH_2O$-2 sample was ~65.35 $m^2/g$ before the photocatalytic reaction, and it was ~65.48 $m^2/g$ after five consecutive cycles. Thus, the crystal structure, morphology, and surface area of the sample were stable during the photocatalytic reaction and regeneration process cycles. Figures 8(c) and 8(d) show high-resolution O 1s and Nb 3d XPS spectraof the $V_O$-$Nb_2O_5$·$nH_2O$-2 sample after five consecutive cycles, respectively. Its oxygen

**Table 2** Photocatalytic nitrogen fixation performances of various photocatalysts reported

| Material system | Light source | Reaction medium | $NH_3$ yield (μmol/(g·h)) | Ref. |
|---|---|---|---|---|
| Fe-doped $TiO_2$ | Full spectrum | Water | 64.2 | [51] |
| Ce-doped BiOCl | 300 W Xe lamp | Water | 46.7 | [52] |
| $In_2S_3$ nanotube | Full spectrum | Water | 52.49 | [53] |
| BiOBr nanosheet | Full spectrum | Water | 54.7 | [54] |
| CuCr-LDH nanosheet | ≥ 400 nm | Water | 57.1 | [55] |
| $Zn_{0.1}Sn_{0.1}Cd_{0.8}S$ | 400–800 nm | **Ethanol** | 131.9 | [56] |
| MIL-101(Fe) | UV–vis | Water | 100.7 | [57] |
| Mn-$W_{18}O_{49}$ microspheres | UV–vis | **$Na_2SO_3$** | 97.9 | [58] |
| Au/$TiO_2$-OVs | ≥ 420 nm | **Methanol** | 78.6 | [59] |
| $Fe_{0.05}$-g-$C_3N_4$ | 400–800 nm | **Ethanol** | 150.0 | [60] |
| TCN/ZnS/$ZnIn_2S_4$ | UV–vis | Water | 68.9 | [61] |
| 7r-PW12/BiOCl-OVs | 300 W Xe lamp | Water | 33.6 | [62] |
| 3% Fe/$Bi_2O_{2.33}$ | 300 W Xe-lamp | Water | 118.7 | [63] |
| Vo-$Nb_2O_5$·$nH_2O$ | 300 W Xe lamp | Water | 173.7 | This work |

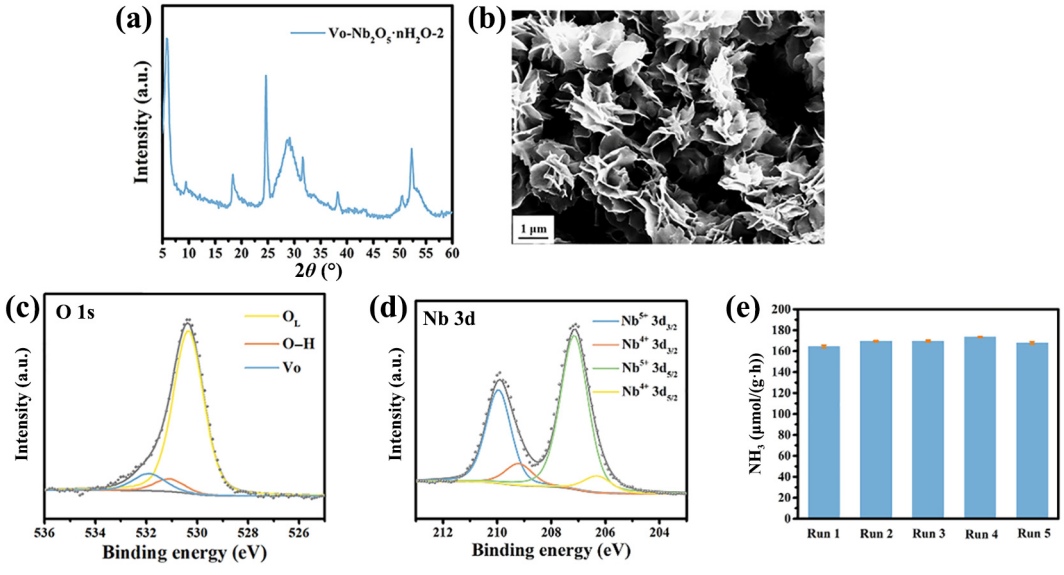


**Fig. 8** (a) XRD pattern and (b) SEM image of $V_O$-$Nb_2O_5$·$nH_2O$-2 sample after five consecutive cycles. High-resolution (c) O 1s and (d) Nb 3d XPS spectra of $V_O$-$Nb_2O_5$·$nH_2O$-2 sample after five consecutive cycles. (e) Average ammonia production rates of five consecutive runs with $V_O$-$Nb_2O_5$·$nH_2O$-2 sample in pure water without assistance of any sacrificial agent or cocatalysts.

vacancy percentage was ~9.60%, and its $Nb^{4+}$ : $Nb^{5+}$ ratio was ~16.38%, both of which are very close to that of its fresh state. Figure 8(e) shows the average ammonia production rates of five consecutive runs by the $V_O$-$Nb_2O_5{\cdot}nH_2O$-2 sample in pure water without the assistance of any sacrificial agent or cocatalysts, which demonstrated that it had relatively stable ammonia production for these consecutive runs. Thus, the regeneration process could effectively refresh the $V_O$-$Nb_2O_5{\cdot}nH_2O$-2 sample to its fresh state for repeated use, indicating its stable performance.

### 3.6 Mechanism investigation of enhanced photocatalytic nitrogen fixation

For a successful photocatalytic nitrogen fixation process, $N_2$ molecules must first be effectively adsorbed on the photocatalyst surface, followed by activation, redox reactions, and product dissociation [5,12]. However, the adsorption and activation of $N_2$ molecules on a photocatalyst's surface are still major problems limiting the photocatalytic nitrogen fixation efficiency at present [5]. Thus, the adsorption and activation of $N_2$ molecules on our samples were first explored to illuminate the effects of oxygen vacancies and surface acidity of $Nb_2O_5{\cdot}nH_2O$. Figure 9 shows$N_2$ TPD curves of the pristine $Nb_2O_5{\cdot}nH_2O$, $V_O$-$Nb_2O_5{\cdot}nH_2O$-2, and $V_O$-$Nb_2O_5{\cdot}nH_2O$-2-300 samples. For the pristine $Nb_2O_5{\cdot}nH_2O$ sample, a broad peak centered at ~105 °C was clearly observed, which could be attributed to the $N_2$ physisorption [16,64,65]. The additional peak of $V_O$-$Nb_2O_5{\cdot}nH_2O$-2 sample at ~275 °C could be attributed to $N_2$ chemisorption [64,65]. The main difference between these two samples was that the $V_O$-$Nb_2O_5{\cdot}nH_2O$-2 sample had a much higher (over two times) oxygen vacancy concentration than the pristine $Nb_2O_5{\cdot}nH_2O$ sample. Thus, this observation indicated that $N_2$ adsorption could be enhanced by the introduction of oxygen vacancies on these $Nb_2O_5{\cdot}nH_2O$ nanosheets. After heat treatment in an Ar atmosphere, the $N_2$ adsorption peak of the $V_O$-$Nb_2O_5{\cdot}nH_2O$-2-300 sample was obviously lower than that of the $V_O$-$Nb_2O_5{\cdot}nH_2O$-2 sample. The oxygen vacancy concentrations were similar, while the $V_O$-$Nb_2O_5{\cdot}nH_2O$-2 sample had a much stronger surface acidity than the $V_O$-$Nb_2O_5{\cdot}nH_2O$-2-300 sample. Thus, the surface acidity also played a major role in the effective $N_2$ adsorption on these $Nb_2O_5{\cdot}nH_2O$ nanosheets.

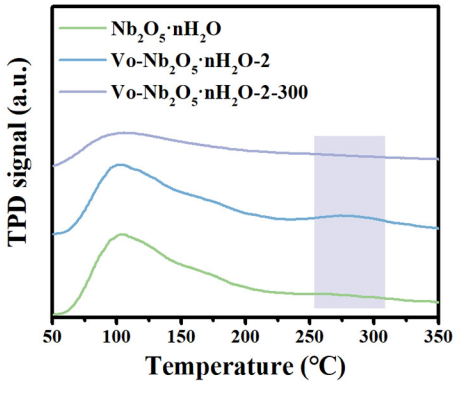


**Fig. 9** $N_2$ TPD curves of pristine $Nb_2O_5{\cdot}nH_2O$, $V_O$-$Nb_2O_5{\cdot}nH_2O$-2, and $V_O$-$Nb_2O_5{\cdot}nH_2O$-2-300 samples.

To ensure efficient photocatalysis, the effective separation and transfer of photogenerated charge carriers are also considered important prerequisites [5,12]. Figure 10(a) compares the Nyquist plots of the $Nb_2O_5{\cdot}nH_2O$, $V_O$-$Nb_2O_5{\cdot}nH_2O$-X, and $V_O$-$Nb_2O_5{\cdot}nH_2O$-2-300 samples obtained from their EIS measurements. The impedance arc radii of these samples followed the order of $V_O$-$Nb_2O_5{\cdot}nH_2O$-2 < $V_O$-$Nb_2O_5{\cdot}nH_2O$-1 < $V_O$-$Nb_2O_5{\cdot}nH_2O$-3 < $V_O$-$Nb_2O_5{\cdot}nH_2O$-2-300 < $Nb_2O_5{\cdot}nH_2O$. In general, the arc radius of the Nyquist plot represents the reaction rate on the electrode surface, and a smaller arc radius indicates better photogenerated charge carrier separation and faster transfer of interfacial charges [66]. Thus, the increase in the oxygen vacancy concentration initially increased the photogenerated charge carrier separation and transfer in these $Nb_2O_5{\cdot}nH_2O$ nanosheets, which subsequently improved the photocatalytic nitrogen fixation performance, as shown in Fig. 7(a). When the oxygen vacancy concentration further increased above the optimal value, too many oxygen vacancies could serve as charge carrier recombination centers [67], which caused an increase in the impedance arc radius and a decrease in the photocatalytic nitrogen fixation performance. After heat treatment, the impedance arc radius of the $V_O$-$Nb_2O_5{\cdot}nH_2O$-2-300 sample was obviously larger than that of the $V_O$-$Nb_2O_5{\cdot}nH_2O$-2 sample, which indicated that a lower surface acidity also caused deteriorated charge carrier separation and transfer. Figure 10(b) shows the photocurrent measurement results of these samples, which were similar to those of the EIS measurements. The results also demonstrated that the photocurrent density initially increased with increasing oxygen vacancy concentration and then decreased when the oxygen vacancy concentration was greater than the optimal value. Furthermore, the photocurrent density of the $V_O$-$Nb_2O_5{\cdot}nH_2O$-2-300 sample decreased sharply from that of the $V_O$-$Nb_2O_5{\cdot}nH_2O$-2 sample, which could be attributed to its largely decreased surface acidity.

Based on above experimental and analysis results, the superior photocatalytic nitrogen fixation performance of the $V_O$-$Nb_2O_5{\cdot}nH_2O$-2 sample could be attributed to the synergistic effect of its rich oxygen vacancies and strong surface acidity. $N_2$ molecules can be efficiently adsorbed and activated on the surface of these $Nb_2O_5{\cdot}nH_2O$ nanosheets because of the existence of oxygen vacancies [18,51,54] and surface acid sites [68–70]. Owing

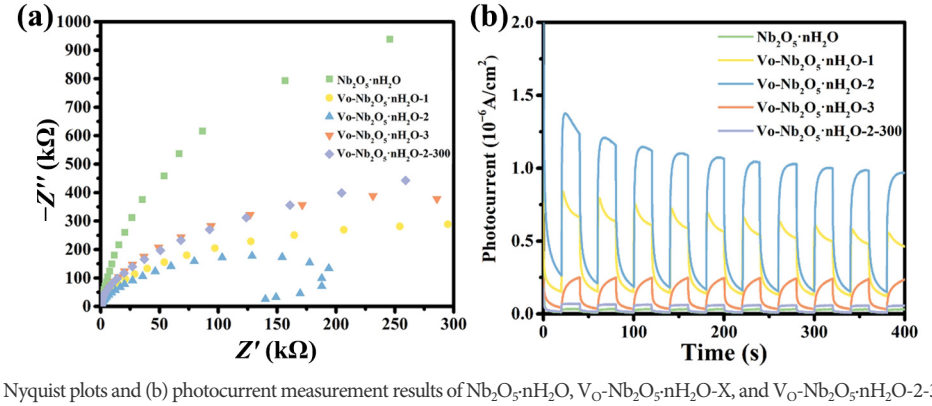


**Fig. 10** (a) Nyquist plots and (b) photocurrent measurement results of $Nb_2O_5{\cdot}nH_2O$, $V_O$-$Nb_2O_5{\cdot}nH_2O$-X, and $V_O$-$Nb_2O_5{\cdot}nH_2O$-2-300 samples.

to its proper electronic band gap structure, it could generate electrons with enough reducing ability to reduce $N_2$ to $NH_3$ and holes with enough oxidizing ability to oxidize $H_2O$ to $O_2$ under simulated solar irradiation. Both of its rich oxygen vacancy and strong surface acidity contributed to its enhanced charge carrier separation and transfer to its surface for the subsequent nitrogen reduction. The photocatalytic reduction of $N_2$ occurred in the distal associative pathway by hydrogenation with $H^+$ from $H_2O$ at the end of the nitrogen molecule far away from the photocatalyst surface. Then, hydrogenation occurred on the other N atoms of the nitrogen molecule in the same way. Finally, the cleavage of the N–N bond of $H_3N$–$NH_3$ generates two $NH_3$ molecules [49–52].

## 4 Conclusions

In summary, $Nb_2O_5{\cdot}nH_2O$ nanosheets with abundant surface oxygen vacancies and strong surface acidity ($V_O$-$Nb_2O_5{\cdot}nH_2O$-2 sample) were created by a hydrothermal reduction process with a weak reducing agent of glyoxal, which largely promoted the separation/migration of charge carriers and the adsorption/activation of $N_2$. Thus, the synergistic effect of both oxygen vacancies and surface acidity largely enhanced the photocatalytic $N_2$ fixation performance of $Nb_2O_5{\cdot}nH_2O$ nanosheets under simulated solar illumination. The average ammonia production rate of the $V_O$-$Nb_2O_5{\cdot}nH_2O$-2 sample reached ~173.7 μmol/(g·h) in pure water without the assistance of any sacrificial agent or co-catalyst, which was approximately 4 times that of the pristine $Nb_2O_5{\cdot}nH_2O$ sample at ~44 μmol/(g·h). This work clearly suggested that the synergistic effect of both surface oxygen vacancies and surface acidity could be readily applied to various metal oxide-based photocatalysts to enhance their photocatalytic $N_2$ fixation performance, and this strategy could also offer good potential for a wide range of applications in photocatalysis.

### Acknowledgements

This study was supported by the National Natural Science Foundation of China (No. 52272125), the Fundamental Research Funds for the Central Universities (No. YX11999123714O1-009), the Youth Science and Technology Innovation Research Team Project of Sichuan Province (No. 2024NSFTD0016), the Science and Technology Program of Guizhou Province(No. [2023]414), and the Research Project of China Three Gorges Co. (No. NBZZ202400321). We would like to thank the Analysis and Testing Center of Southwest Jiaotong University for the assistance on material characterization.

### Availability of data and materials

The data that support the findings of this study are available from the corresponding author upon reasonable request.

### Competing interests

The authors have no competing interests to declare that are relevant to the content of this article. The author Qi Li is the Editorial Committee member of this journal.

### Electronic Supplementary Material

Supplementary material is available in the online version of this article at https://doi.org/10.26599/JAC.2025.9221070.

### References

[1] Canfield DE, Glazer AN, Falkowski PG. The evolution and future of Earth's nitrogen cycle. *Science* 2010, **330**: 192–196.

[2] Stüeken EE, Boocock T, Szilas K, *et al.* Reconstructing nitrogen sources to earth's earliest biosphere at 3.7 Ga. *Front Earth Sci* 2021, **9**: 675726.

[3] Kandemir T, Schuster DME, Senyshyn DA, *et al.* The Haber–Bosch process revisited: On the real structure and stability of "ammonia iron" under working conditions. *Angew Chem Int Ed* 2013, **52**: 12723–12726.

[4] Foster SL, Bakovic SIP, Duda RD, *et al.* Catalysts for nitrogen reduction to ammonia. *Nat Catal* 2018, **1**: 490–500.

[5] Medford AJ, Hatzell MC. Photon-driven nitrogen fixation: Current progress, thermodynamic considerations, and future outlook. *ACS Catal* 2017, **7**: 2624–2643.

[6] Gong YT, Li HC, Li C, *et al.* Insight into rare-earth-incorporated catalysts: The chance for a more efficient ammonia synthesis. *J Adv Ceram* 2022, **11**: 1499–1529.

[7] Schrauzer GN, Guth TD. Photolysis of water and photoreduction of nitrogen on titanium dioxide. *J Am Chem Soc* 1977, **99**: 7189–7193.

[8] Ye LQ, Han CQ, Ma ZY, *et al.* $Ni_2P$ loading on $Cd_{0.5}Zn_{0.5}S$ solid solution for exceptional photocatalytic nitrogen fixation under visible light. *Chem Eng J* 2017, **307**: 311–318.

[9] Wang JP, Fang YX, Zhang WX, *et al.* $TiO_2$/BiOBr 2D–2D heterostructure via *in situ* approach for enhanced visible-light photocatalytic $N_2$ fixation. *Appl Surf Sci* 2021, **567**: 150623.

[10] Chem ORD, Dr AEP, Dr GF, *et al.* Nitrogen photofixation at nanostructured iron titanate films. *Angew Chem Int Ed* 2001, **40**: 3993–3995.

[11] Hu SZ, Li YM, Li FY, *et al.* Construction of g-$C_3N_4$/$Zn_{0.11}Sn_{0.12}Cd_{0.88}S_{1.12}$ hybrid heterojunction catalyst with outstanding nitrogen photofixation performance induced by sulfur vacancies. *ACS Sustain Chem Eng* 2016, **4**: 2269–2278.

[12] Chen ST, Liu D, Peng TY. Fundamentals and recent progress of photocatalytic nitrogen-fixation reaction over semiconductors. *Sol RRL* 2021, **5**: 2000487.

[13] Chen XZ, Li N, Kong ZZ, *et al.* Photocatalytic fixation of nitrogen to ammonia: State-of-the-art advancements and future prospects. *Mater Horiz* 2018, **5**: 9–27.

[14] Shen HD, Yang MM, Hao LD, *et al.* Photocatalytic nitrogen reduction to ammonia: Insights into the role of defect engineering in photocatalysts. *Nano Res* 2022, **15**: 2773–2809.

[15] Li HM, Shen QQ, Zhang H, *et al.* Oxygen vacancy-mediated $WO_3$ phase junction to steering photogenerated charge separation for enhanced water splitting. *J Adv Ceram* 2022, **11**: 1873–1888.

[16] Wang SY, Hai X, Ding X, *et al.* Light-switchable oxygen vacancies in ultrafine $Bi_5O_7Br$ nanotubes for boosting solar-driven nitrogen fixation in pure water. *Adv Mater* 2017, **29**: 1701774.

[17] Li G, Yang WY, Gao S, *et al.* Creation of rich oxygen vacancies in bismuth molybdate nanosheets to boost the photocatalytic nitrogen fixation performance under visible light illumination. *Chem Eng J* 2021, **404**: 127115.

[18] Zhang YT, Ran L, Zhang YX, *et al.* Two-dimensional defective boron-doped niobic acid nanosheets for robust nitrogen photofixation. *ACS Nano* 2021, **15**: 17820–17830.

[19] Sun ML, Zhang WD, Sun YJ, *et al.* Synergistic integration of metallic Bi and defects on BiOI: Enhanced photocatalytic NO removal and conversion pathway. *Chin J Catal* 2019, **40**: 826–836.

[20] Yu HJ, Chen F, Li XW, *et al.* Synergy of ferroelectric polarization and oxygen vacancy to promote $CO_2$ photoreduction. *Nat Commun* 2021, **12**: 4594.

[21] Lin MY, An BX, Niimi N, *et al.* Role of the acid site for selective catalytic oxidation of $NH_3$ over Au/$Nb_2O_5$. *ACS Catal* 2019, **9**: 1753–1756.

[22] Cui H, Dwight K, Soled S, *et al.* Surface acidity and photocatalytic activity of $Nb_2O_5$/$TiO_2$ photocatalysts. *J Solid State Chem* 1995, **115**: 187–191.

[23] Zhang HY, Gao S, Guan HT, *et al.* Highly selective photocatalytic $CO_2$ reduction to ethylene in pure water by $Nb_2O_5$ nanoparticles with enriched surface –OH groups under simulated solar illumination. *J Adv Ceram* 2023, **12**: 1641–1654.

[24] Chen JL, Wang H, Zhang ZQ, *et al.* Ultrathin $HNb_3O_8$ nanosheets with oxygen vacancies for enhanced photocatalytic oxidation of amines under visible light irradiation. *J Mater Chem A* 2019, **7**: 5493–5503.
[25] Zhao Y, Zhou XW, Ye L, *et al.* Nanostructured $Nb_2O_5$ catalysts. *Nano Rev* 2012, **3**: 17631.
[26] Nakajima K, Baba Y, Noma R, *et al.* $Nb_2O_5{\cdot}nH_2O$ as a heterogeneous catalyst with water-tolerant Lewis acid sites. *J Am Chem Soc* 2011, **133**: 4224–4227.
[27] da Silva GTST, Nogueira AE, Oliveira JA, *et al.* Acidic surface niobium pentoxide is catalytic active for $CO_2$ photoreduction. *Applied Catal B—Environ* 2019, **242**: 349–357.
[28] Furukawa S, Ohno Y, Shishido T, *et al.* Reaction mechanism of selective photooxidation of amines over niobium oxide: Visible-light-induced electron transfer between adsorbed amine and $Nb_2O_5$. *J Phys Chem C* 2013, **117**: 442–450.
[29] Fan WQ, Zhang QH, Deng WP, *et al.* Niobic acid nanosheets synthesized by a simple hydrothermal method as efficient Brønsted acid catalysts. *Chem Mater* 2013, **25**: 3277–3287.
[30] Zhou L, Boyd CE. Comparison of Nessler, phenate, salicylate and ion selective electrode procedures for determination of total ammonia nitrogen in aquaculture. *Aquaculture* 2016, **450**: 187–193.
[31] Dambrauskas T, Cornish HH. A modified spectrophotometric method for the determination of hydrazine. *Am Ind Hyg Assoc J* 1962, **23**: 151–156.
[32] Takagaki A, Tagusagawa C, Hayashi S, *et al.* Nanosheets as highly active solid acid catalysts for green chemical syntheses. *Energy Environ Sci* 2010, **3**: 82–93.
[33] Yang DM, Shen DL, Lu YY, *et al.* Disorder engineering in monolayer nanosheets enabling photothermic catalysis for full solar spectrum (250–2500 nm) harvesting. *Angew Chem Int Ed* 2019, **58**: 3077–3081.
[34] Yu HJ, Li JY, Zhang PY, *et al.* Three-in-one oxygen vacancies: Whole visible-spectrum absorption, efficient charge separation, and surface site activation for robust $CO_2$ photoreduction. *Angew Chem Int Ed* 2019, **58**: 3880–3884.
[35] Hong ZH, Shen B, Chen YL, *et al.* Enhancement of photocatalytic $H_2$ evolution over nitrogen-deficient graphitic carbon nitride. *J Mater Chem A* 2013, **1**: 11754–11761.
[36] Zhang HM, Wang Y, Liu PR, *et al.* Highly ordered single crystalline nanowire array assembled three-dimensional $Nb_3O_7(OH)$ and $Nb_2O_5$ superstructures for energy storage and conversion applications. *ACS Nano* 2016, **10**: 507–514.
[37] Zhou P, Li QJ, He J, *et al.* Structural features of $HNb_3O_8$ nanosheets and their catalytic performance in toluene nitration. *Russ J Phys Chem A* 2015, **89**: 2097–2104.
[38] Su KY, Liu HF, Zeng B, *et al.* Visible-light-driven selective oxidation of toluene into benzaldehyde over nitrogen-modified $Nb_2O_5$ nanomeshes. *ACS Catal* 2020, **10**: 1324–1333.
[39] Liang DS, Wen LR, Lin DS, *et al.* Monolayer $HNb_3O_8$ for selective photocatalytic oxidation of benzylic alcohols with visible light response. *Angew Chem Int Ed* 2014, **126**: 2995–2999.
[40] Liu H, Zhang HT, Shen P, *et al.* Synergistic effects in nanoengineered $HNb_3O_8$/graphene hybrids with improved photocatalytic conversion ability of $CO_2$ into renewable fuels. *Langmuir* 2016, **32**: 254–264.
[41] Florentino A, Cartraud P, Magnoux P, *et al.* Textural, acidic and catalytic properties of niobium phosphate and of niobium oxide Influence of the pretreatment temperature. *Appl Catal A—Gen* 1992, **89**: 143–153.
[42] Tauc J, Grigorovici R, Vancu A. Optical properties and electronic structure of amorphous germanium. *Phys Status Solidi* 1966, **15**: 627–637.
[43] Uddin MT, Nicolas Y, Olivier C, *et al.* Nanostructured $SnO_2$–ZnO heterojunction photocatalysts showing enhanced photocatalytic activity for the degradation of organic dyes. *Inorg Chem* 2012, **51**: 7764–7773.
[44] Wang M, Shen M, Jin XX, *et al.* Oxygen vacancy generation and stabilization in $CeO_{2-x}$ by Cu introduction with improved $CO_2$ photocatalytic reduction activity. *ACS Catal* 2019, **9**: 4573–4581.
[45] Tu WG, Xu Y, Wang JJ, *et al.* Investigating the role of tunable nitrogen vacancies in graphitic carbon nitride nanosheets for efficient visible-light-driven $H_2$ evolution and $CO_2$ reduction. *ACS Sustain Chem Eng* 2017, **5**: 7260–7268.
[46] Xia DP, Cao PS, Zhu DB, *et al.* Designing a 0D/2D S-scheme heterojunction over polymeric carbon nitride for visible-light photocatalytic inactivation of bacteria. *Angew Chem Int Ed* 2020, **59**: 5218–5225.
[47] Chen SS, Qi Y, Liu GJ, *et al.* A wide visible-light-responsive tunneled $MgTa_2O_{6-x}N_x$ photocatalyst for water oxidation and reduction. *Chem Commun* 2014, **50**: 14415–14417.
[48] Zhao YX, Shi R, Bian XA, *et al.* Ammonia detection methods in photocatalytic and electrocatalytic experiments: How to improve the reliability of $NH_3$ production rates. *Adv Sci* 2019, **6**: 1802109.
[49] Huang YW, Zhang N, Wu ZJ, *et al.* Artificial nitrogen fixation over bismuth-based photocatalysts: Fundamentals and future perspectives. *J Mater Chem A* 2020, **8**: 4978–4995.
[50] Zhao JX, Chen ZF. Single Mo atom supported on defective boron nitride monolayer as an efficient electrocatalyst for nitrogen fixation: A computational study. *J Am Chem Soc* 2017, **139**: 12480–12487.
[51] Bo YN, Wang HY, Lin DY, *et al.* Altering hydrogenation pathways in photocatalytic nitrogen fixation by tuning local electronic structure of oxygen vacancy with dopant. *Angew Chem Int Ed* 2021, **60**: 16085–16092.
[52] Li HY, Wang JR, Ruan Z, *et al.* Electron transfer bridge inducing polarization of nitrogen molecules for enhanced photocatalytic nitrogen fixation. *Mater Horiz* 2023, **10**: 5053–5059.
[53] He ZY, Wang Y, Dong XL, *et al.* Indium sulfide nanotubes with sulfur vacancies as an efficient photocatalyst for nitrogen fixation. *RSC Adv* 2019, **9**: 21646–21652.
[54] Xue XL, Chen RP, Chen HW, *et al.* Oxygen vacancy engineering promoted photocatalytic ammonia synthesis on ultrathin two-dimensional bismuth oxybromide nanosheets. *Nano Lett* 2018, **18**: 7372–7377.
[55] Zhao YF, Zhao YX, Waterhouse GIN, *et al.* Layered-double-hydroxide nanosheets as efficient visible-light-driven photocatalysts for dinitrogen fixation. *Adv Mater* 2017, **29**: 1703828.
[56] Hu SZ, Chen X, Li Q, *et al.* Effect of sulfur vacancies on the nitrogen photofixation performance of ternary metal sulfide photocatalysts. *Catal Sci Technol* 2016, **6**: 5884–5890.
[57] Li GQ, Li FF, Liu JX, *et al.* Fe-based MOFs for photocatalytic $N_2$ reduction: Key role of transition metal iron in nitrogen activation. *J Solid State Chem* 2020, **285**: 121245.
[58] Ying ZH, Chen ST, Zhang S, *et al.* Efficiently enhanced $N_2$ photofixation performance of sea-urchin-like $W_{18}O_{49}$ microspheres with Mn-doping. *Appl Catal B—Environ* 2019, **254**: 351–359.
[59] Yang JH, Guo YZ, Jiang RB, *et al.* High-efficiency "working-in-tandem" nitrogen photofixation achieved by assembling plasmonic gold nanocrystals on ultrathin titania nanosheets. *J Am Chem Soc* 2018, **140**: 8497–8508.
[60] Hu SZ, Chen X, Li Q, *et al.* $Fe^{3+}$ doping promoted $N_2$ photofixation ability of honeycombed graphitic carbon nitride: The experimental and density functional theory simulation analysis. *Appl Catal B—Environ* 2017, **201**: 58–69.
[61] Sun T, Gao P, He YQ, *et al.* Dual *Z*-scheme TCN/ZnS/$ZnIn_2S_4$ with efficient separation for photocatalytic nitrogen fixation. *J Colloid Interf Sci* 2024, **654**: 602–611.
[62] Sun ML, Zhang RY, Sun A, *et al.* Heteropoly blue-modified ultrathin bismuth oxychloride nanosheets with oxygen vacancies for efficient photocatalytic nitrogen fixation in pure water. *J Colloid Interf Sci* 2025, **677**: 610–619.
[63] Zhu CY, Zhang LL, Cui LY, *et al.* Fe–Bi dual sites regulation of $Bi_2O_{2.33}$ nanosheets to promote photocatalytic nitrogen fixation activity. *J Colloid Interface Sci* 2024, **661**: 46–58.

[64] Dong GH, Ho W, Wang CY. Selective photocatalytic $N_2$ fixation dependent on g-$C_3N_4$ induced by nitrogen vacancies. *J Mater Chem A* 2015, **3**: 23435–23441.
[65] Nowak I, Ziolek M. Niobium compounds: Preparation, characterization, and application in heterogeneous catalysis. *Chem Rev* 1999, **99**: 3603–3624.
[66] Jia HM, Zhang BB, He WW, *et al*. Mechanistic insights into the photoinduced charge carrier dynamics of BiOBr/CdS nanosheet heterojunctions for photovoltaic application. *Nanoscale* 2017, **9**: 3180–3187.
[67] Liu LJ, Jiang YQ, Zhao HL, *et al*. Engineering coexposed {001} and {101} facets in oxygen-deficient $TiO_2$ nanocrystals for enhanced $CO_2$ photoreduction under visible light. *ACS Catal* 2016, **6**: 1097–1108.
[68] Ran Y, Yu XL, Liu JQ, *et al*. Polymeric carbon nitride with frustrated Lewis pair sites for enhanced photofixation of nitrogen. *J Mater Chem A* 2020, **8**: 13292–13298.
[69] Yu XM, Han P, Wei ZX, *et al*. Boron-doped graphene for electrocatalytic $N_2$ reduction. *Joule* 2018, **2**: 1610–1622.
[70] Sun X, Jiang D, Zhang L, *et al*. Enhanced nitrogen photofixation over $LaFeO_3$ via acid treatment. *ACS Sustain Chem Eng* 2017, **5**: 9965–9971.